



LAWRENCE
LIVERMORE
NATIONAL
LABORATORY

Thomson scattering in the average-atom approximation

W. R. Johnson, J. Nilsen, K. T. Cheng

June 28, 2012

Physical Review E

Disclaimer

This document was prepared as an account of work sponsored by an agency of the United States government. Neither the United States government nor Lawrence Livermore National Security, LLC, nor any of their employees makes any warranty, expressed or implied, or assumes any legal liability or responsibility for the accuracy, completeness, or usefulness of any information, apparatus, product, or process disclosed, or represents that its use would not infringe privately owned rights. Reference herein to any specific commercial product, process, or service by trade name, trademark, manufacturer, or otherwise does not necessarily constitute or imply its endorsement, recommendation, or favoring by the United States government or Lawrence Livermore National Security, LLC. The views and opinions of authors expressed herein do not necessarily state or reflect those of the United States government or Lawrence Livermore National Security, LLC, and shall not be used for advertising or product endorsement purposes.

Thomson scattering in the average-atom approximation

W. R. Johnson*

*Department of Physics, 225 Newland Science Hall
University of Notre Dame, Notre Dame, IN 46556*

J. Nilsen and K. T. Cheng (鄭國錚)

Lawrence Livermore National Laboratory, Livermore CA 94551

The average-atom model is applied to study Thomson scattering of x-rays from warm-dense matter with emphasis on scattering by bound electrons. Parameters needed to evaluate the dynamic structure function (chemical potential, average ionic charge, free electron density, bound and continuum wave-functions and occupation numbers) are obtained from the average-atom model. The resulting analysis provides a relatively simple diagnostic for use in connection with x-ray scattering measurements. Applications are given to dense hydrogen, beryllium, aluminum and titanium plasmas. In the case of titanium, bound states are predicted to modify the spectrum significantly.

PACS numbers: 52.65.Rr, 52.70.-m, 52.38.-r, 52.25.Os, 52.27.Gr, 52.25.Mq

I. INTRODUCTION

Measurements of Thomson scattering of x-rays provide information on temperatures, densities and ionization balance in warm dense matter. Various techniques for inferring plasma properties from x-ray scattering measurements have been developed over the past decade [1–22]; these techniques together with the underlying theory were reviewed by Glenzer and Redmer [23]

The present analysis of Thomson scattering from dense plasmas is based on a theoretical model proposed by Gregori et al. [3], one important difference being that the parameters used here to evaluate the Thomson-scattering dynamic structure function are taken from the average-atom model. The particular average-atom model used here is described in [24]. The present work is closely related to that of Sahoo et al. [25], where a somewhat different version of the average-atom model was used. Predictions from the present model differ substantially from those in [25]. The origin and consequences of these differences will be discussed later.

The Thomson scattering cross section for an incident photon with energy, momentum (ω_0 , \mathbf{k}_0) and polarization ϵ_0 scattering to a state with energy, momentum (ω_1 , \mathbf{k}_1) and polarization ϵ_1 is

$$\frac{d\sigma}{d\omega_1 d\Omega} = \left(\frac{d\sigma}{d\Omega} \right)_{\text{Th}} \frac{\omega_1}{\omega_0} S(k, \omega), \quad (1)$$

where

$$\left(\frac{d\sigma}{d\Omega} \right)_{\text{Th}} = |\epsilon_0 \cdot \epsilon_1|^2 \left(\frac{e^2}{mc^2} \right)^2. \quad (2)$$

The *dynamic structure function* $S(k, \omega)$ appearing in Eq. (1) depends on two variables: $k = |\mathbf{k}_0 - \mathbf{k}_1|$ and

$\omega = \omega_0 - \omega_1$. As shown in the seminal work of Chihara [26, 27], $S(k, \omega)$ can be decomposed into three terms: the first $S_{ii}(k, \omega)$ is the contribution from elastic scattering by electrons that follow the ion motion, the second $S_{ee}(k, \omega)$ is the contribution from scattering by free electrons and the third $S_B(k, \omega)$ is the contribution from bound-free transitions (inelastic scattering by bound electrons) modulated by the ionic motion. In the present work, the modulation factor is ignored when evaluating the bound-free scattering structure function. For the bound-free contribution, calculations carried out using plane-wave final states are compared with calculations carried out using average-atom scattering wave functions. Substantial differences are found between these cases.

The average-atom model is discussed briefly in Sec. II followed by a discussion of the three contributions to the structure functions in Sec. III. In Sec. IV applications are given to hydrogen, beryllium, aluminum and titanium plasmas.

II. AVERAGE-ATOM MODEL

The average-atom model is a quantum mechanical version of the temperature-dependent Thomas-Fermi model of a plasma developed sixty-three years ago by Feynman et al. [28]. In this model, the plasma is divided into neutral Wigner-Seitz (WS) cells (volume per atom $V_{\text{ws}} = A/\rho N_A$, where A is the atomic weight, ρ is the mass density and N_A is Avogadro's number). Inside each WS cell is a nucleus of charge Z and Z electrons. Some of these electrons are in bound states and some in continuum states. The continuum density is finite at the cell boundary and merges into the uniform free-electron density Z_f/V_{ws} outside the cell. Each neutral cell can, therefore, be regarded as an ion imbedded in a uniform sea of free electrons of density $n_e = Z_f/V_{\text{ws}}$. To maintain overall neutrality, it is necessary to introduce a uniform (but inert) positive background density Z_f/V_{ws} . The model,

*Electronic address: johnson@nd.edu

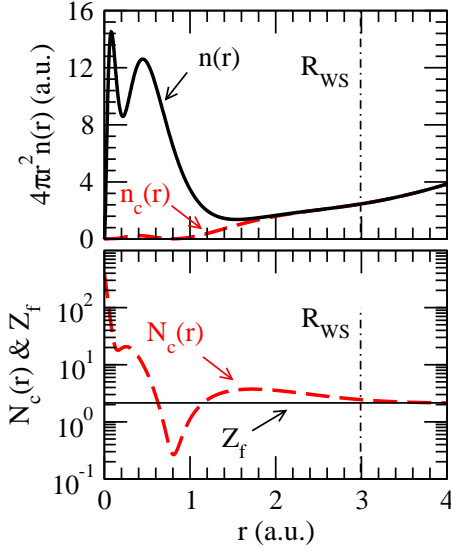


FIG. 1: (Color online) Upper panel: The radial density $4\pi r^2 n(r)$ for metallic Al at $k_B T = 5$ eV (solid curve) integrates to $Z = 13$ for $r \leq R_{ws}$. The continuum contribution $4\pi r^2 n_c(r)$ (dashed curve) integrates to 3 for $r \leq R_{ws}$. The bound $1s$, $2s$ and $2p$ shells are completely occupied at this temperature. Lower panel: The dashed curve illustrates the Friedel oscillations of the continuum density and shows how $N_c(r) = n_c(r)V_{ws}$ converges to $Z_f = n_e V_{ws}$ (solid line) for $r > R_{ws}$. The chemical potential predicted by the model is $\mu = 0.2406$ a.u. and the number of free electrons per ion is $Z_f = 2.146$.

therefore, describes an isolated (neutral) ion floating in a (neutral) “jellium” sea.

The quantum-mechanical model here, which is discussed in Ref. [24], is a nonrelativistic version of the relativistic *Inferno* model of Liberman [29] and the more recent *Purgatorio* model of Wilson et al. [30]; it is similar to the nonrelativistic average-atom model described by Blenski and Ishikawa [31]. Specifically, each electron in the ion is assumed to satisfy the central-field Schrödinger equation

$$\left[\frac{p^2}{2} - \frac{Z}{r} + V \right] \psi_a(\mathbf{r}) = \epsilon_a \psi_a(\mathbf{r}), \quad (3)$$

where $a = (n, l)$ for bound states or (ϵ, l) for continuum states. Atomic units (a.u.) where $e = \hbar = m = 1$ are used here. In particular, 1 a.u. in energy equals 2 Rydbergs (27.211 eV), and 1 a.u. in length equals 1 Bohr radius a_0 (0.529 Å). The wave function $\psi_a(\mathbf{r})$ is decomposed in a spherical basis as

$$\psi_a(\mathbf{r}) = \frac{1}{r} P_a(r) Y_{l_a m_a}(\hat{r}) \chi_{\sigma_a}, \quad (4)$$

where $Y_{lm}(\hat{r})$ is a spherical harmonic and χ_{σ} is a 2-component electron spinor. The bound and continuum

radial functions $P_a(r)$ are normalized as

$$\int_0^\infty dr P_{nl}(r) P_{n'l}(r) = \delta_{nn'}, \quad (5)$$

$$\int_0^\infty dr P_{\epsilon l}(r) P_{\epsilon' l}(r) = \delta(\epsilon - \epsilon'), \quad (6)$$

respectively. The central potential $V(r)$ in Eq. (1) is taken to be the self-consistent Kohn-Sham potential [32]

$$V(r) = 4\pi \int \frac{1}{r_{>}} r'^2 n(r') dr' - x_\alpha \left[\frac{81}{8\pi} n(r) \right]^{\frac{1}{3}}, \quad (7)$$

where the first term in the R.H.S. is the direct screening potential with $r_{>} = \max(r, r')$ and the second term is the average exchange potential with $x_\alpha = 2/3$. The electron density $n(r)$ in Eq. (7) has contributions from bound-states $n_b(r)$ and from continuum states $n_c(r)$,

$$n(r) = n_b(r) + n_c(r). \quad (8)$$

The bound-state contribution to the density $n_b(r)$ is

$$4\pi r^2 n_b(r) = \sum_{nl} \frac{2(2l+1)}{1 + \exp[(\epsilon_{nl} - \mu)/k_B T]} P_{nl}(r)^2, \quad (9)$$

where ϵ_{nl} is the bound-state energy, μ is the chemical potential, and the sum over (n, l) ranges over all bound subshells. The continuum contribution to the density $n_c(r)$ is given by a similar expression with the bound state radial functions $P_{nl}(r)$ replaced by continuum functions $P_{\epsilon l}(r)$ and the sum over n replaced by an integral over ϵ . Finally, the chemical potential μ is chosen to insure charge neutrality inside the WS cell:

$$Z = \int_{r \leq R_{ws}} n(r) d^3 r \equiv \int_0^{R_{ws}} 4\pi r^2 n(r) dr. \quad (10)$$

Equations (3-10) above are solved self-consistently to give the chemical potential μ , the potential $V(r)$ and the electron density $n(r)$.

The boundary conditions used in solving Eq. (3) deserve some mention. Bound state wave functions and their derivatives are matched at the boundary $r = R_{ws}$ to solutions outside the WS sphere (where $V = 0$) that vanish exponentially as $r \rightarrow \infty$. Similarly, continuum functions and their derivatives are matched to phase-shifted free-particle wave functions at $r = R_{ws}$. It should be noticed that the continuum density $n_c(r)$ inside the WS sphere, which oscillates as predicted by Friedel [33], is distinctly different from the uniform free electron density n_e . In the present model, $n_c(r)$ smoothly approaches n_e outside the sphere. These points are illustrated in Fig. 1, where the bound-state and continuum densities are plotted for Al at metallic density and temperature $k_B T = 5$ eV.

The boundary conditions used here differ from those used by Sahoo et al. in Ref. [25], where the first derivative of the wave function is required to vanish at R_{ws} . The

differences in boundary conditions lead to major differences in the average-atom structure. For example, the model used in [25] predicts that the M-shell of metallic Al is partially occupied at temperatures $k_B T \leq 10$ eV, whereas the present model predicts that the M-shell is empty in this temperature range. Consequences of such differences are discussed later in Sec. IV.

III. DYNAMIC STRUCTURE FUNCTION

In the paragraphs below, the evaluation of $S(k, \omega)$ in the average-atom approximation is discussed. As mentioned earlier, the theoretical model developed by Gregori et al. [3] is used to evaluate the ion-ion contribution $S_{ii}(k, \omega)$ to the dynamic structure function. Additionally, the procedure proposed in Ref. [8] is used to account for differences between electron and ion temperatures. The electron-electron contribution $S_{ee}(k, \omega)$ is expressed in terms of the dielectric function $\epsilon(k, \omega)$ of the free electrons which in turn is evaluated using the random-phase approximation (RPA). Finally, bound-state contributions to the dynamic structure function are evaluated using average-atom bound state wave functions. The final-state wave function is described in two different ways: (1) using a plane-wave final-state wave function as in Ref. [25], and (2) using an average-atom final-state wave function that approaches a plane wave asymptotically. There are dramatic differences between these choices. The more realistic average-atom choice automatically includes ionic Coulomb-field effects.

A. Ion-Ion Structure Function

The contribution to the dynamic structure function from elastic scattering by electrons following the ion motion $S_{ii}(k, \omega)$ is expressed in terms of the corresponding static ion-ion structure function $S_{ii}(k)$ as:

$$S_{ii}(k, \omega) = |f(k) + q(k)|^2 S_{ii}(k) \delta(\omega). \quad (11)$$

In the above, $f(k)$ is the Fourier transform of the bound-state density and $q(k)$ is the Fourier transform of electrons that screen the ionic charge. In the average-atom approximation, the screening electrons are the continuum electrons inside the Wigner-Seitz sphere and

$$f(k) + q(k) = 4\pi \int_0^{R_{WS}} r^2 [n_b(r) + n_c(r)] j_0(kr) dr, \quad (12)$$

where $j_l(z)$ are spherical Bessel functions of order l . Note that $f(0) + q(0) = Z$ in the average-atom model. Furthermore, the delta function $\delta(\omega)$ in Eq. (11) is replaced by an “instrumental” Gaussian, with full-width at half maximum = 10 eV in this work.

Approximate schemes to evaluate the static structure functions $S_{ii}(k)$ are discussed, for example, in Ref. [34]. Here, we follow [3] and make use of formulas given

by Arkhipov and Davletov [35] that account for both quantum-mechanical and screening effects. The function $S_{ii}(k)$ in [35] is expressed in terms of the Fourier transform of the ion-ion interaction potential $\Phi_{ii}(r)$ through the relation:

$$S_{ii}(k) = 1 - \frac{n_i}{k_B T} \Phi_{ii}(k). \quad (13)$$

Different Electron and Ion Temperatures In the average atom model, T is the electron temperature T_e which, in equilibrium, is equal to the ion temperature T_i . To allow for different electron and ion temperatures, the equations for $S_{ii}(k)$ given by Arkhipov and Davletov [35] are modified following the prescription laid out by Gregori et al. [8]. The electron temperature T_e is replaced by an effective temperature T'_e that accounts for degeneracy effects at temperatures lower than the Fermi temperature T_F . Similarly, the ion temperature T_i is replaced by an effective temperature T'_i that accounts for ion degeneracy effects at temperatures lower than the ion screened Debye temperature T_D . Explicit formulas for $S_{ii}(k)$ are found in [8]. The dramatic effect of different electron and ion temperatures on the static structure functions $S_{ii}(k)$ for metallic Be at $T_e = 20$ eV are illustrated in the top panel of Fig. 2. This figure is similar to the upper-left panel of Fig. 1 in Ref. [8], which was obtained under similar condition. In the bottom panel of Fig. 2 the contribution to $S_{ii}(k, \omega)$ for Be at $T_e = 20$ eV and $T_i = 2$ eV is shown.

B. Electron-Electron Structure Function

The electron-electron structure function $S_{ee}(k, \omega)$ is expressed in terms of the plasma dielectric function $\epsilon(k, \omega)$ through Eq. (15) in Ref. [3]:

$$S_{ee}(k, \omega) = -\frac{1}{1 - \exp(-\omega/k_B T)} \frac{k^2}{4\pi n_e} \text{Im} \left[\frac{1}{\epsilon(k, \omega)} \right]. \quad (14)$$

In the average atom model, the free electrons are uniformly distributed outside the WS sphere. The density of these electrons is $n_e = Z_f/V_{WS}$. In the present work, the dielectric function is evaluated using the random-phase approximation. The real and imaginary parts of the RPA dielectric function $\epsilon(k, \omega)$, given in Eq. (16) of Ref. [3], can be written as

$$\begin{aligned} \text{Re}[\epsilon(k, \omega)] &= 1 + \frac{2}{\pi k^3} \int_0^\infty \mathcal{F}(p) p dp \\ &\times \left[\ln \left| \frac{k^2 + 2pk + 2\omega}{k^2 - 2pk + 2\omega} \right| + \ln \left| \frac{k^2 + 2pk - 2\omega}{k^2 - 2pk - 2\omega} \right| \right] \end{aligned} \quad (15)$$

and

$$\begin{aligned} \text{Im}[\epsilon(k, \omega)] &= \frac{2}{k^3} \int_a^b \mathcal{F}(p) p dp \\ &= \frac{2k_B T}{k^3} \log \left[\frac{1 + \exp[(\mu - a^2/2)/k_B T]}{1 + \exp[(\mu - b^2/2)/k_B T]} \right] \end{aligned} \quad (16)$$

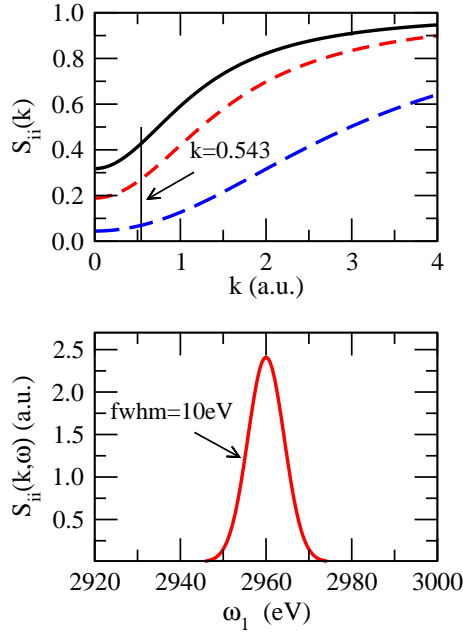


FIG. 2: (Color online) Upper panel: $S_{ii}(k)$ is shown for Be metal at electron temperature $T_e=20$ eV and ion-electron temperature ratios $T_i/T_e=(1, 0.5, 0.1)$ illustrated in solid, short dashed and long dashed curves, respectively. The value $k = 0.543$ corresponds to an incident photon $\omega_0 = 2960$ eV scattered at angle 40° . Lower panel: $S_{ii}(k, \omega)$ for Be metal at $T_e = 20$ eV and $T_i = 2$ eV, where the function $\delta(\omega)$ is replaced by a Gaussian of width 10 eV and $k = 0.543$.

with $a = |2\omega - k^2|/2k$ and $b = (2\omega + k^2)/2k$. In these equations,

$$\mathcal{F}(p) = \frac{1}{1 + \exp[(p^2/2 - \mu)/k_B T]} \quad (17)$$

is the free-electron Fermi distribution function. It should be noted that the real part of $\epsilon(k, \omega)$ is an even function of ω and the imaginary part is an odd function of ω .

The real and imaginary parts of $\epsilon(k, \omega)$ along with $-\text{Im}[1/\epsilon(k, \omega)]$ are illustrated in the top panel of Fig. 3 for scattering of a 2960 eV photon at 20° from Be metal at 20 eV. The sharp peak in $\text{Im}[1/\epsilon]$ that occurs near the point where $\text{Re}[\epsilon]$ vanishes is a collective plasma resonance (plasmon). The contribution to $S_{ee}(k, \omega)$ is shown in the bottom panel. The ratio of the down-shifted ($\omega_1 < 2960$ eV) to up-shifted ($\omega_1 > 2960$ eV) resonance peaks $\exp(\Delta\omega/k_B T)$, where $\Delta\omega$ is the energy of the plasmon peak relative to the central energy, is used to determine the electron temperature.

C. Scattering from Bound States

The structure function associated with Thomson scattering from a bound state $\psi_{nl}(\mathbf{r})$ with quantum numbers

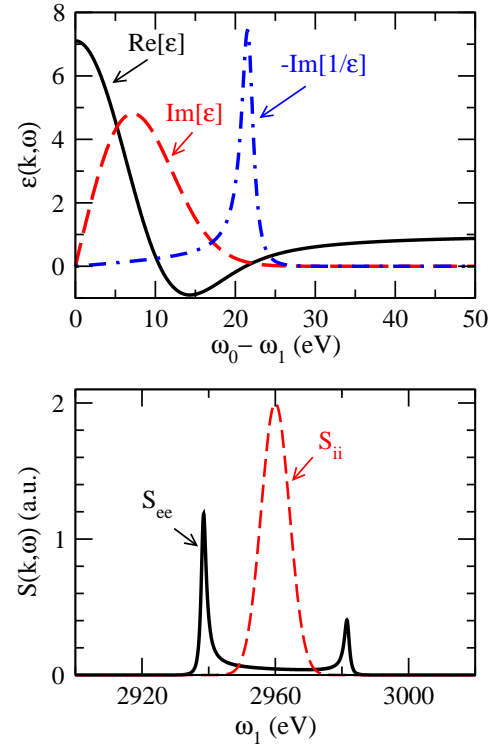


FIG. 3: (Color online) Upper panel: Real (solid) and imaginary (dashed) parts of $\epsilon(k, \omega)$ are plotted along with $\text{Im}[1/\epsilon(k, \omega)]$ (dot-dashed) for Be metal at $k_B T = 20$ eV. Lower panel: The resulting structure function $S_{ee}(k, \omega)$ (solid) is shown together with $S_{ii}(k, \omega)$ (dashed). These plots correspond to Thomson scattering of a 2960eV photon at 20° .

(n, l) to a continuum state $\psi_p(\mathbf{r})$ with momentum \mathbf{p} is

$$S_{nl}(k, \omega) = \sum_m \int \frac{p d\Omega_p}{(2\pi)^3} \int d^3r \psi_p^\dagger(\mathbf{r}) e^{i\mathbf{k}\cdot\mathbf{r}} \psi_{nlm}(\mathbf{r}) \Big|_{E_p=\omega+E_{nl}}^2. \quad (18)$$

As mentioned previously, two possibilities are considered for the final state in bound-free scattering: (1) a free-particle plane wave, and (2) an average-atom continuum wave that approaches a plane wave asymptotically. Case (2) is clearly the more physical alternative since continuum waves in the average-atom potential differ markedly from free-particle wave functions. This point is illustrated in Fig. 4, where the average atom radial functions $P_\ell(r)/pr$ are compared with their free-particle counterparts $j_\ell(pr)$. The average-atom wave functions are seen to differ markedly from the free-particle (spherical Bessel) functions for low values of l , but approach free-particle functions as l increases.

a. Plane-wave final states Assuming that the final state wave function is a free-particle plane wave $e^{i\mathbf{p}\cdot\mathbf{r}}$, the bound-free structure function in Eq. (18) can be rewritten

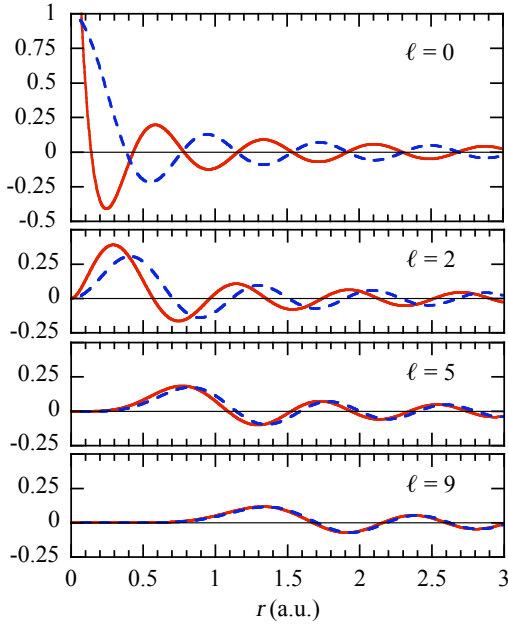


FIG. 4: (Color online) Comparison of average-atom continuum functions $P_l(pr)/pr$ (solid lines) for metallic Al at $k_B T = 5$ eV with spherical Bessel functions $j_l(pr)$ (dashed lines).

ten as

$$S_{nl}(k, \omega) = \sum_m \int \frac{p d\Omega_p}{(2\pi)^3} \left| \int d^3r e^{i\mathbf{q} \cdot \mathbf{r}} \psi_{nlm}(\mathbf{r}) \right|_{Ep=\omega+E_{nl}}^2, \quad (19)$$

where $\mathbf{k} = \mathbf{k}_0 - \mathbf{k}_1$, $\omega = \omega_0 - \omega_1$ and $\mathbf{q} = \mathbf{k} - \mathbf{p}$. Note that \mathbf{q} is the momentum transferred to the ion. This expression may be simplified to

$$S_{nl}(k, \omega) = \frac{o_{nl}}{\pi k} \int_{|p-k|}^{p+k} q dq |K_{nl}(q)|^2, \quad (20)$$

where o_{nl} is the occupation number of the final state and

$$K_{nl}(q) = \int_0^\infty dr r j_l(qr) P_{nl}(r). \quad (21)$$

Eq. (20) depends implicitly on ω through the relation

$$p = \sqrt{2(\omega + E_{nl})}.$$

b. Average-atom final states In the average-atom approach, the final state wave function consists of a plane wave plus an *incoming* spherical wave. (n.b. An outgoing spherical wave is associated with an incident electron. Time-reversal invariance, therefore, requires that a converging spherical wave be associated with an emerging electron.) The bound-free structure function in Eq. (18) may be reexpressed as

$$S_{nl} = \frac{2p}{\pi} o_{nl} \sum_{l_1 l_2} A_{l_1 l_2} |I_{l_1 l_2}(p, k)|^2, \quad (22)$$

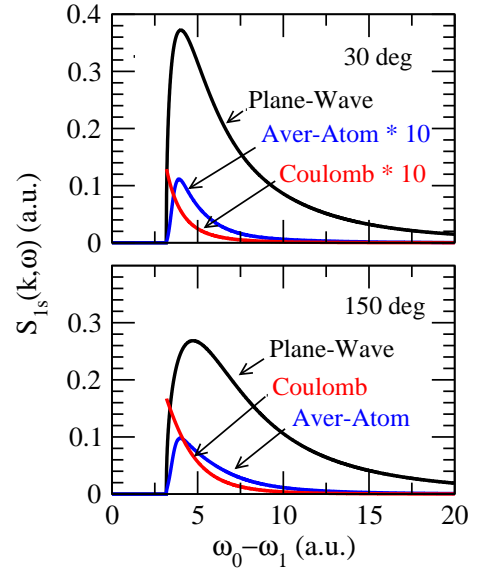


FIG. 5: (Color online) The beryllium K-shell structure function $S_{1s}(k, \omega)$ is shown for incident photon energy 2960 eV and scattering angles 30° and 150° . The black curves show plane-wave results, the blue lines show the result obtained using an average atom final-state wave function and the red lines show exact nonrelativistic Coulomb results. The dramatic suppression of average atom and Coulomb structure functions at forward angles (the corresponding curves are multiplied by 10) is evident in the upper panel.

where o_{nl} is the occupation number of the final state with

$$I_{l_1 l_2}(p, k) = \frac{1}{p} e^{i\delta_{l_1}(p)} \int_0^{R_{ws}} dr P_{\epsilon l_1}(r) j_{l_2}(kr) P_{nl}(r). \quad (23)$$

and

$$A_{l_1 l_2} = (2l_1 + 1)(2l_2 + 1) \begin{pmatrix} l_1 & l & l_2 \\ 0 & 0 & 0 \end{pmatrix}. \quad (24)$$

In the above, $\delta_{l_1}(p)$ is the phase-shift of the final state partial wave $P_{\epsilon l_1}(r)$. Moreover, $\epsilon = \omega + E_{nl}$, $p = \sqrt{2\epsilon}$ and $k = |\mathbf{k}_0 - \mathbf{k}_1|$.

In Fig. 5, several calculations of the structure function $S_{1s}(k, \omega)$ are compared for a photon of incident energy 2960 eV scattered at 30° and 150° from the K-shell of beryllium metal at $T = 20$ eV. The results of calculations carried out using average-atom final states are smaller than those using plane-wave final states by a factor of about 40 at forward angles and 2.5 at backward angles. This suppression is a characteristic Coulomb field effect. Indeed, exact nonrelativistic Coulomb-field calculations of Thomson scattering [36], with nuclear charge adjusted to align the Coulomb and average atom thresholds, show a similar suppression.

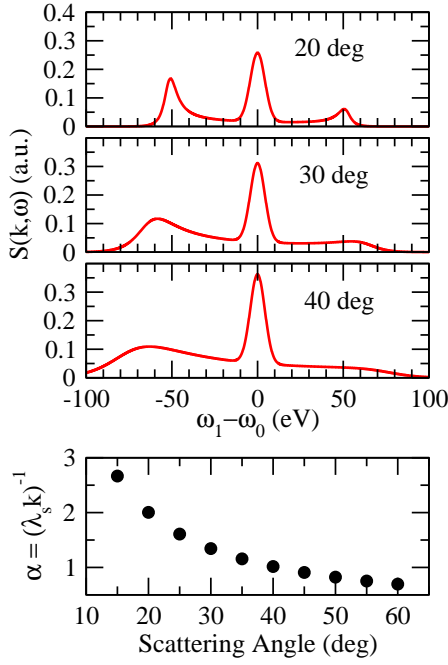


FIG. 6: (Color online) The evolution of plasmon resonances for scattering of a 5 keV photon from a fully ionized dense H plasma ($T = 50$ eV, $n_e = 10^{24}$ cm $^{-3}$) is illustrated in the top panel where we plot $S(k, \omega)$ for scattering angles of 20° , 30° and 40° . The corresponding coherence parameters $\alpha = 1/\lambda_s k$ are plotted in the bottom panel.

IV. APPLICATIONS

In the subsections below, $S(k, \omega)$ is evaluated in the average-atom approximation for cases of possible experimental interest: hydrogen at $n_e = 10^{24}$ cm $^{-3}$ and $T = 50$ eV, beryllium at $n_e = 1.8 \times 10^{23}$ cm $^{-3}$ and $T = 18$ eV, metallic aluminum at $T = 5$ eV and metallic titanium at $T = 10$ eV.

A. Hydrogen at $T = 50$ eV and $n_e = 10^{24}$ cm $^{-3}$

In the average-atom model, a density $\rho = 1.931$ g/cc is required at $T = 50$ eV to achieve free-electron density $n_e = 10^{24}$ cm $^{-3}$. The chemical potential in this case is $\mu = -1.091$ (a.u.). Under these conditions of temperature and density, hydrogen is completely ionized. The continuum density $n_c(r)$ inside the WS sphere merges into the free-electron density n_e outside the sphere. The total number of electrons inside the WS sphere $N_c = 4\pi \int_0^{R_{WS}} r^2 n_c(r) dr = 1$, however, $Z_f = 0.8667$.

Since there are no bound electrons in this case, only S_{ii} and S_{ee} contribute to the cross section. Dynamic structure functions for scattering of a 5 keV photon at angles ranging from 20° , 30° and 40° are shown in the top panel of Fig. 6. Resonance peaks are seen to broaden and move to higher frequencies as the scattering angle increases. The coherence parameter $\alpha = 1/(\lambda_s k)$, defined

in Eqs. (5-7) of Ref. [23], is plotted in the bottom panel of Fig. 6. The parameter λ_s is the shielding length, given by

$$\lambda_s = \sqrt{\frac{k_B T F_{1/2}(\mu/k_B T)}{4\pi n_e F_{-1/2}(\mu/k_B T)}}, \quad (25)$$

where $F_j(x)$ is a complete Fermi-Dirac integral,

$$F_\nu(x) = \frac{1}{\Gamma(1+\nu)} \int_0^\infty \frac{y^\nu}{1 + \exp(y-x)} dy. \quad (26)$$

For this particular case, $\lambda_s = 1.071$ (a.u.). The value of λ_s differs only slightly from the WS radius $R_{WS} = 1.118$ a.u.. The resonant features in Fig. 6 are distinct for $\alpha > 1$ but disappear for $\alpha \leq 1$, in harmony with the fact that plasmon resonances are collective phenomena. It should be noted that the (unperturbed) plasma frequency for hydrogen at $n_e = 10^{24}$ cm $^{-3}$ is $\omega_{pl} = 37.1$ eV.

B. Beryllium at $T = 18$ eV and $n_e = 1.8 \times 10^{23}$ cm $^{-3}$

In the bottom panel of Fig. 7, the structure function for scattering of a 2963 eV photon at 40° from beryllium (density = 1.636 g/cc) at $T_e = 18$ eV is plotted. The L-shell electrons are completely stripped under these conditions but the K-shell remains 97% occupied. The chemical potential is $\mu = -0.5311$ a.u. and the number of free electrons per ion $Z_f = 1.647$. The ion temperature, which governs the amplitude of the elastic peak, is chosen to be $T_i = 2.1$ eV in this example. For the case at hand, the coherence parameter is $\alpha = 1.21$, so one expects and observes plasmon peaks in the scattering intensity profile. The average-atom removal energy for a K-shell electron is 86.8 eV. One therefore expects to find a contribution to $S(k, \omega)$ from K-shell electrons for energies $\omega_1 < 2876$ eV. The K-shell contribution multiplied by 50 is shown in the bottom panel.

To validate the present average-atom model against experimental data, a Be experiment done at the Omega laser facility that used a Cl Ly- α source to scatter from nearly solid Be at an angle of 40° is used. An electron temperature of 18 eV, ion temperature of 2.1 eV, and density of 1.647 g/cc used in the average-atom model gives an electron density of 1.8×10^{23} /cc, in agreement with the analysis in Ref. [37]. The top panel of Fig. 7 shows the experimental source function from the Cl Ly- α line as a blue dashed line. Because of satellite structure in the source we approximate the source by 3 lines: a Cl Ly- α line at 2963 eV with amplitude 1 and two satellites at 2934 and 2946 eV with relative amplitudes of 0.075 and 0.037 respectively. Doing the Thomson scattering calculation using the 3 weighted lines, we calculate the scattering amplitude for Thomson scattering (red dashed line) and compare against the experimental data (black solid line) here. We observe excellent agreement within the experimental noise. Contributions from the bound 1s

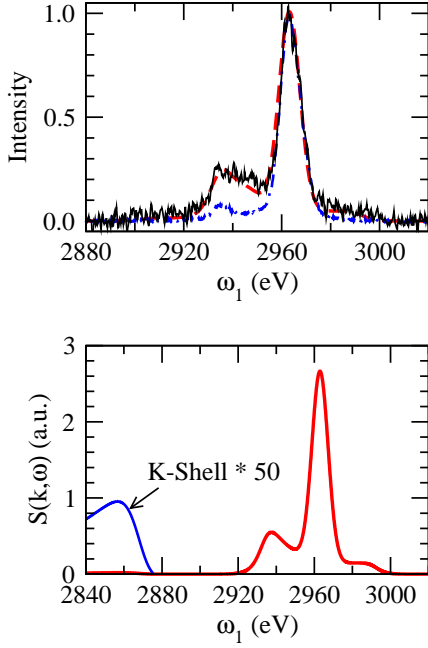


FIG. 7: (Color online) Bottom panel: Structure function $S(k, \omega)$ for scattering of a 2963 eV photon at 40° from metallic beryllium at $T_e = 18$ eV. Top panel: Intensity measurements for scattering of a Cl Ly- α x-ray from beryllium at 40° [37]; measurement (solid line), source function (dot-dashed line), and average atom fit (dashed line).

electrons, which have a threshold at 2876 eV, are beyond the range of the data shown in the top panel.

C. Aluminum at $T = 5$ eV and metallic density

Metallic aluminum ($\rho = 2.70$ gm/cc) at $T = 5$ eV has a Ne-like ion configuration with two $2s$ electrons bound by 92.2 eV and six $2p$ electrons bound by 54.9 eV. There are three continuum electrons inside the WS sphere $R_{ws} = 2.99$ (a.u.). The continuum density inside the sphere $n_c(r)$ converges to the uniform free-electron density $n_e = Z_f/V_{WK}$, where $Z_f = 2.146$. In Fig. 8, the structure function $S(k, \omega)$ is plotted for the case of an incident 2.96 keV photon scattered at 30° . The coherence parameter $\alpha = 1.95$ in this case, explaining the prominent plasmon resonance seen on the low-frequency side of the elastic scattering peak. Also shown in the figure are contributions from the bound L-shell electrons scaled up by a factor of 100. It should be noted that, by contrast with the average-atom calculations presented in Ref. [25], the M shell of Al is completely empty at temperatures below 10 eV in the present model and the prominent M -shell features predicted in Ref. [25] do not arise in the present analysis.

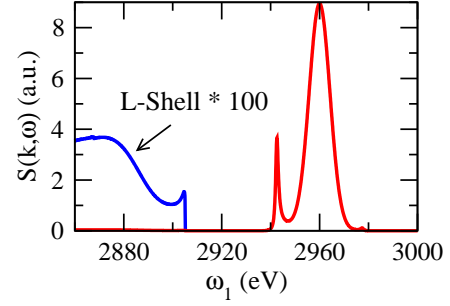


FIG. 8: (Color online) Structure function $S(k, \omega)$ for scattering of an 8 keV photon at 30° from metallic aluminum ($Z = 13$) at $T_e = 5$ eV and $T_i/T_e = 0.1$. Contributions from the L-shell of the Ne-like core multiplied by 100 are indicated on the plot.

D. Titanium at $T = 10$ eV and metallic density

Titanium ($Z = 22$) at metallic density ($\rho = 4.51$ g/cc) and $T = 10$ eV is a case where sharp peaks from excitations of bound M-shell electrons show up in the energy spectrum along with the plasmon peaks. The average-atom model predicts that metallic Ti is in an Ar-like configuration at $T = 10$ eV with completely filled K and L shells together with 1.97 $3s$ electrons bound by 44.40 eV and 5.36 $3p$ electrons bound by 22.88 eV. There are 4.67 continuum electrons inside the WS sphere $R_{ws} = 3.05$ (a.u.). The continuum density inside the sphere converges to the uniform free-electron density $n_e = Z_f/V_{WK}$ outside the sphere, with $Z_f = 2.305$. The chemical potential is $\mu = -0.0511$ au. In Fig. 9, the dynamic structure function $S(k, \omega)$ is shown for the case of an incident 2.96 keV photon scattered at 30° and 150° . Plasmon peaks, which are prominent for scattering at 30° , disappear for scattering at 150° while the $3s$ and $3p$ bound-state peaks grow. The M-shell contributions to the structure function are comparable to the plasmon contribution for the 30° case and are the dominant features on the low-frequency side of the elastic peak at 150° .

V. SUMMARY

A scheme for analysis of Thomson scattering from plasmas based on the average-atom model, a quantum-mechanical version of the “Generalized Thomas-Fermi Theory” of Feynman, Metropolis and Teller [28] is presented. Given the plasma composition (Z, A), density ρ and temperature T , the model gives, in addition to the equation of state of the plasma, all parameters needed for a complete description of the Thomson scattering process. In particular, the average-atom code predicts wave functions for bound and continuum electrons, densities of bound, screening and free electrons, and the chemical potential.

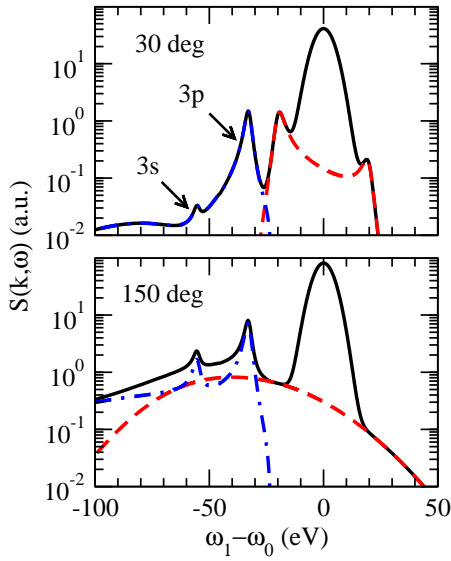


FIG. 9: (Color online) Dynamic structure function $S(k, \omega)$ for scattering of a 2960 eV photon at 30° and 150° from metallic Ti at $T_e = 10$ eV. Contributions to $S(k, \omega)$ (solid curve) from $S_{ee}(k, \omega)$ (dashed curve) and $S_B(k, \omega)$ (dot-dashed curve) are shown.

Predictions of the present average-atom model disagree with those in [25] where a similar model with different boundary conditions is used. In particular, in Ref. [25], 3d electrons were bound in metallic Al for temperatures between 2 and 10 eV, leading to substantial bound-state contributions to the dynamic structure function. In the present model the 3d subshell of metallic aluminum is vacant in the temperature range $T \leq 10$ eV and the corresponding bound-state features are absent.

Elastic scattering from bound and screening electrons is treated following the model proposed by Gregori et al.

[3] which makes use of formulas for the static ion-ion structure function $S_{ii}(k)$ given by Arkhipov and Davletov [35]. Modifications suggested by Gregori et al. [8] to account for different electron and ion temperatures are also included. Treatment of the ion-ion structure function appears to be the weakest aspect of the present analysis. The dynamic structure function for scattering from free electrons depends sensitively on the free-electron dielectric function $\epsilon(k, \omega)$. Again, we follow the model proposed in Ref. [3] and evaluate the dielectric function in the random-phase approximation. The RPA dielectric function includes features such as plasmon resonant peaks that show up in experimental intensity profiles and can be used in connection with the principle of detailed balance to determine electron temperatures. Bound-state features are included in the present scheme, inasmuch as the average-atom model provides bound-state and continuum wave functions. Coulomb-field effects are automatically included in calculations carried out using average-atom continuum states rather than plane waves to describe the final state electron. In conclusion, the average-atom model provides a simple and consistent point of departure for theoretical analysis of Thomson scattering from plasmas.

Acknowledgements

We owe debts of gratitude to S. H. Glenzer, C. Fortmann and T. Döppner for informative discussions and for providing comparison experimental data for x-ray scattering from beryllium. The work of J.N. and K.T.C. was performed under the auspices of the U.S. Department of Energy by Lawrence Livermore National Laboratory under Contract DE-AC52-07NA27344.

-
- [1] G. Gregori, S. Glenzer, R. Lee, D. Hicks, J. Pasley, G. Collins, P. Celliers, M. Bastea, J. Eggert, S. Pollaine, et al., in *Spectral Line Shapes*, edited by C. Back (2002), vol. 645 of *AIP Conference Proceedings*, pp. 359–368.
 - [2] R. Lee, H. Baldi, R. Cauble, O. Landen, J. Wark, A. Ng, S. Rose, C. Lewis, D. Riley, J. Gauthier, et al., *Laser Part. Beams* **20**, 527 (2002).
 - [3] G. Gregori, S. H. Glenzer, W. Rozmus, R. W. Lee, and O. L. Landen, *Phys. Rev. E* **67**, 026412 (2003).
 - [4] R. Lee, S. Moon, H. Chung, W. Rozmus, H. Baldi, G. Gregori, R. Cauble, O. Landen, J. Wark, A. Ng, et al., *J. Opt. Soc. Am. B* **20**, 770 (2003).
 - [5] S. H. Glenzer, G. Gregori, R. W. Lee, F. J. Rogers, S. W. Pollaine, and O. L. Landen, *Phys. Rev. Lett.* **90**, 175002 (2003).
 - [6] G. Gregori, S. Glenzer, and O. Landen, *J. Phys. A* **36**, 5971 (2003).
 - [7] A. Holl, R. Redmer, G. Röpke, and H. Reinholz, *Eur. Phys. J. D* **29**, 159 (2004).
 - [8] G. Gregori, S. H. Glenzer, and O. L. Landen, *Phys. Rev. E* **74**, 026402 (2006).
 - [9] S. H. Glenzer, O. L. Landen, P. Neumayer, R. W. Lee, K. Widmann, S. W. Pollaine, R. J. Wallace, G. Gregori, A. Hoell, T. Bornath, et al., *Phys. Rev. Lett.* **98**, 065002 (2007).
 - [10] R. Thiele, T. Bornath, C. Fortmann, A. Hoell, R. Redmer, H. Reinholz, G. Röpke, A. Wierling, S. H. Glenzer, and G. Gregori, *Phys. Rev. E* **78**, 026411 (2008).
 - [11] A. L. Kritcher, P. Neumayer, H. J. Lee, T. Döppner, R. W. Falcone, S. H. Glenzer, and E. C. Morse, *Rev. Sci. Instrum.* **79**, 10E739 (2008).
 - [12] R. R. Faeustlin, S. Toleikis, T. Bornath, L. Cao, T. Döppner, S. Düsterer, E. Foerster, C. Fortmann, S. H. Glenzer, S. Goede, et al., in *Ultrafast Phenomena XVI*, edited by P. Corkum, S. DeSilvestri, K. Nelson, and E. Riedle (2009), vol. 92 of *Springer Series in Chemical Physics*, pp. 241–243, 16th International Conference on Ultrafast Phenomena,

- European Phys Soc, Stresa, Italy, Jun. 09-13, 2008.
- [13] T. Döppner, O. L. Landen, H. J. Lee, P. Neumayer, S. P. Regan, and S. H. Glenzer, *High Energy Density Phys.* **5**, 182 (2009).
 - [14] N. L. Kugland, G. Gregori, S. Bandyopadhyay, C. M. Brenner, C. R. D. Brown, C. Constantin, S. H. Glenzer, F. Y. Khattak, A. L. Kritcher, C. Niemann, et al., *Phys. Rev. E* **80**, 066406 (2009).
 - [15] S. H. Glenzer, H. J. Lee, P. Davis, T. Döppner, R. W. Falcone, C. Fortmann, B. A. Hammel, A. L. Kritcher, O. L. Landen, R. W. Lee, et al., *High Energy Density Phys.* **6**, 1 (2010).
 - [16] M. S. Murillo, *Phys. Rev. E* **81**, 036403 (2010).
 - [17] S. Toleikis, T. Bornath, T. Döppner, S. Duesterer, R. R. Faeustlin, E. Foerster, C. Fortmann, S. H. Glenzer, S. Goede, G. Gregori, et al., *J. Phys. B* **43**, 194017 (2010), ISSN 0953-4075.
 - [18] R. Redmer and G. Roepke, *Contrib. Plasm. Phys.* **50**, 970 (2010).
 - [19] A. L. Kritcher, T. Döppner, C. Fortmann, O. L. Landen, R. Wallace, and S. H. Glenzer, *High Energy Density Phys.* **7**, 271 (2011).
 - [20] A. J. Visco, R. P. Drake, S. H. Glenzer, T. Döppner, G. Gregori, D. H. Froula, and M. J. Grosskopf, *Phys. Rev. Lett.* **108**, 145001 (2012).
 - [21] C. Fortmann, H. J. Lee, T. Döppner, R. W. Falcone, A. L. Kritcher, O. L. Landen, C. Niemann, and S. H. Glenzer, *Contrib. Plasma Phys.* **52**, 186 (2012).
 - [22] U. Zastra, T. Burian, J. Chalupsky, T. Döppner, T. W. J. Dzelzainis, R. R. Faeustlin, C. Fortmann, E. Galtier, S. H. Glenzer, G. Gregori, et al., *Laser Part. Beams* **30**, 45 (2012).
 - [23] S. H. Glenzer and R. Redmer, *Rev. Mod. Phys.* **81**, 1625 (2009).
 - [24] W. R. Johnson, C. Guet, and G. F. Bertsch, *J. Quant. Spectros. & Radiat. Transfer* (2006).
 - [25] S. Sahoo, G. F. Gribakin, G. Shabbir Naz, J. Kohanoff, and D. Riley, *Phys. Rev. E* **77**, 046402 (2008).
 - [26] J. Chihara, *J. Phys. F: Met. Phys.* **17**, 295 (1987).
 - [27] J. Chihara, *J. Phys.: Condens. Matter* **12**, 231 (2000).
 - [28] R. P. Feynman, N. Metropolis, and E. Teller, *Phys. Rev.* **75**, 1561 (1949).
 - [29] D. A. Liberman, *Phys. Rev. B* **20**, 4981 (1979).
 - [30] B. Wilson, V. Sonnad, P. Sterne, and W. Isaacs, *J. Quant. Spectros. Radiat. Transfer* **99**, 658'679 (2006).
 - [31] T. Blenski and K. Ishikawa, *Phys. Rev. E* **51**, 4869 (1995).
 - [32] W. Kohn and L. J. Sham, *Phys. Rev.* **140**, A1133 (1965).
 - [33] J. Friedel, *Adv. Phys.* **3**, 507 (1954).
 - [34] J.-P. Hansen and I. R. McDonald, *Theory of Simple Liquids* (Academic, London, Orlando, 2006), 3rd ed.
 - [35] Y. Arkhipov and A. Davletov, *Phys. Letts. A* **227**, 339 (1998).
 - [36] P. Eisenberger and P. M. Platzman, *Phys. Rev. A* **2**, 415 (1970).
 - [37] S. H. Glenzer and T. Döppner (2012), private communication.